

Effect of alumina on photocatalytic activity of iron oxides for bisphenol A degradation

F. B. Li^{1,2#}, X. Z. Li^{1*}, C. S. Liu², T. X. Liu²

¹ Department of Civil and Structural Engineering, The Hong Kong Polytechnic University, Kowloon, Hong Kong, China.

² Guangdong Key Laboratory of Agricultural Environment Pollution Integrated Control, Guangdong Institute of Eco-Environment and Soil Science, Guangzhou, 510650, China.

Abstract

To study the photodegradation of organic pollutants at the interface of minerals and water in natural environment, three series of alumina-coupled iron oxides ($\text{Al}_2\text{O}_3\text{-Fe}_2\text{O}_3\text{-300}$, $\text{Al}_2\text{O}_3\text{-Fe}_2\text{O}_3\text{-420}$, and $\text{Al}_2\text{O}_3\text{-Fe}_2\text{O}_3\text{-550}$) with different alumina fraction were prepared and characterized by X-ray diffraction (XRD), Brunauer-Emmett-Teller (BET) and Barret-Joyner-Halender (BJH), and Fourier transform infrared spectra (FTIR). The XRD results showed that existence of alumina in iron oxides could hinder the formation of maghemite and hematite, and also the crystal transformation from maghemite to hematite during sintering. It has been confirmed that the BET surface area and micropore surface area of $\text{Al}_2\text{O}_3\text{-Fe}_2\text{O}_3$ catalysts increased with an increased dosage of alumina and with decreased sintering temperature. The pore size distribution also depended on the fraction of alumina. Furthermore, all $\text{Al}_2\text{O}_3\text{-Fe}_2\text{O}_3$ catalysts had a mixed pore structure of micropore, mesopore and macropore. FTIR results showed that FTIR peaks attributable to Fe-O vibrations of maghemite or hematite were also affected by alumina content and sintering temperature. It was confirmed that the crystal structure and crystalline, the surface area and pore size distribution of $\text{Al}_2\text{O}_3\text{-Fe}_2\text{O}_3$ catalysts depend strongly on the content of alumina and also sintering temperature. Bisphenol A (BPA) was selected as a model endocrine disruptor in aquatic environment. The effects of alumina on the photocatalytic activity of iron oxides for BPA degradation were investigated in aqueous suspension. The experimental results showed that the dependence of BPA degradation on the alumina content was attributable to the crystal structure, crystalline and also the properties of their surface structures. It was confirmed that the mixed crystal structure of maghemite and hematite could achieve the higher photocatalytic activity than maghemite or hematite alone.

Keywords: Alumina; Bisphenol A; Hematite; Iron oxides; Maghemite; Photodegradation

* Corresponding author: phone: (852) 2766 6016; Fax: (852) 2334 6389; Email: cexzli@polyu.edu.hk
First author's email: cefbli@soil.gd.cn

34 1. Introduction

35
36 Since soil and water on the earth surface suffer from contamination of organic pollutants
37 extensively at different degrees from ppb to ppm levels, it has become important to better
38 understand some abiotic transformations of these organic pollutants naturally occurring in the
39 environment, such as some catalytic processes at mineral surfaces. Actually these processes may
40 play a vital role in decontamination and mineralization of organic pollutants under a natural
41 condition [1-3]. It is necessary to investigate the catalytic properties and activity of these
42 minerals in such catalytic processes. Since these catalytic processes involve some complicated
43 heterogeneous reactions between minerals and water, the interactive reactions occurring at the
44 mineral-water interface become critical to influence the processes of decontamination in the
45 natural environment [4-7].

46 Iron oxides, including oxyhydroxides, are a kind of natural minerals and geocatalysts,
47 naturally existing in the earth's crust with great content [8]. Since these iron oxides are very
48 reactive, a number of secondary iron oxides such as maghemite ($\gamma\text{-Fe}_2\text{O}_3$), hematite ($\alpha\text{-Fe}_2\text{O}_3$),
49 lepidocrocite ($\gamma\text{-FeOOH}$), goethite ($\alpha\text{-FeOOH}$), ferrihydrite ($\text{Fe}_3\text{HO}_8\cdot 4\text{H}_2\text{O}$), and magnetite
50 (Fe_3O_4) were found in aqueous streams as suspended materials with a significant amount [1-3].
51 Hence, the iron oxides in aquatic ecosystems play a vital role in a variety of chemical and
52 biological processes relevant to the transformation of organic compounds.

53 $\gamma\text{-Fe}_2\text{O}_3$ and $\alpha\text{-Fe}_2\text{O}_3$ are two common iron oxides to show semiconductor properties with
54 a narrow band gap of 2.0-2.3 eV and might be photoactive under solar irradiation as
55 photocatalysts or photosensitizers [9,10] as described by the equations 1-3.



(3)

57
58 It has been widely recognized that the iron oxide surface may play an important role as
59 catalysts for photochemical transformations [14-16]. Cunningham et al. [17] obtained the
60 evidence of the photocatalytic formation of $\cdot\text{OH}$ radical in aqueous suspensions of $\alpha\text{-FeOOH}$
61 under visible illumination, even though the photochemical transformation rate for organic
62 degradation was found to be at a lower level. On the other hand, different Fe_2O_3 as natural
63 minerals exist in our natural environment usually not alone and they very often coexist with
64 silicate and alumina in soil. The fraction of silicate and alumina in clay varies in a board range

65 from very low up to 75% [1-3]. However, these silicate and alumina are normally not
66 photoactive under light irradiation at a wavelength of longer than 200 nm owing to their wide
67 band gaps. Meanwhile, alumina-supported iron oxides were also investigated extensively as a
68 kind of industrial catalysts [18-20].

69 In this study, three series of alumina-iron oxide ($\text{Al}_2\text{O}_3\text{-Fe}_2\text{O}_3$) samples with different
70 fraction of alumina up to 70% were prepared as photocatalysts and their photocatalytic activity
71 was evaluated in the degradation of bisphenol A (BPA) as a model endocrine disrupting
72 chemical (EDC) in aqueous solution under UV-A illumination to study the effects of alumina on
73 the photocatalytic activity of iron oxides, since BPA has been extensively used as a raw material
74 of epoxy and polycarbonate resins, and also as antioxidants in softeners, fungicides, and similar
75 products at about 1,700 tons annually all over the world [21,22].

76

77 **2. Experimental Section**

78

79 **2.1 Preparation of Fe_2O_3 and $\text{Al}_2\text{O}_3\text{-Fe}_2\text{O}_3$ powders**

80 Three Fe_2O_3 powder samples were first prepared from $\text{Fe}(\text{NO}_3)_3 \cdot 9\text{H}_2\text{O}$ and glycol by a
81 sol-gel procedure that 0.1 mol of $\text{Fe}(\text{NO}_3)_3 \cdot 9\text{H}_2\text{O}$ was dissolved into 160 ml of glycol and stirred
82 sufficiently; then the solution was refluxed in a 250 ml flask at 65°C for 24 h to get hydrosol; the
83 hydrosol was dried at 100°C for 24 h to obtain xerogel; then the xerogel was ground and
84 sintered at 300°C , 420°C , and 550°C for 2 h, respectively. The 3 product Fe_2O_3 powders were
85 named “ $\text{Fe}_2\text{O}_3\text{-300}$ ” “ $\text{Fe}_2\text{O}_3\text{-420}$ ” and “ $\text{Fe}_2\text{O}_3\text{-550}$ ”.

86 Three series of $\text{Al}_2\text{O}_3\text{-Fe}_2\text{O}_3$ powders were then prepared from $\text{Fe}(\text{NO}_3)_3 \cdot 9\text{H}_2\text{O}$,
87 $\text{Al}(\text{NO}_3)_3 \cdot 9\text{H}_2\text{O}$, and glycol by the similar procedure, in which 0.1 mol of mixture of
88 $\text{Fe}(\text{NO}_3)_3 \cdot 9\text{H}_2\text{O}$ and $\text{Al}(\text{NO}_3)_3 \cdot 9\text{H}_2\text{O}$ was dissolved into 160 ml of glycol with different molar
89 ratios of $\text{Al}/(\text{Fe}+\text{Al})$. The first series of $\text{Al}_2\text{O}_3\text{-Fe}_2\text{O}_3$ powder samples with the alumina contents
90 of 70%, 60%, 50%, 40%, 30%, 20%, 10% and 5% were sintered at 300°C for 2 h and named
91 “ $\text{Al}_2\text{O}_3(0.7)\text{-Fe}_2\text{O}_3\text{-300}$ ”, “ $\text{Al}_2\text{O}_3(0.6)\text{-Fe}_2\text{O}_3\text{-300}$ ”, “ $\text{Al}_2\text{O}_3(0.5)\text{-Fe}_2\text{O}_3\text{-300}$ ”, “ $\text{Al}_2\text{O}_3(0.4)\text{-Fe}_2\text{O}_3\text{-}$
92 300 ”, “ $\text{Al}_2\text{O}_3(0.3)\text{-Fe}_2\text{O}_3\text{-300}$ ”, “ $\text{Al}_2\text{O}_3(0.2)\text{-Fe}_2\text{O}_3\text{-300}$ ”, “ $\text{Al}_2\text{O}_3(0.1)\text{-Fe}_2\text{O}_3\text{-300}$ ”, and
93 “ $\text{Al}_2\text{O}_3(0.05)\text{-Fe}_2\text{O}_3\text{-300}$ ”. Then other two series of $\text{Al}_2\text{O}_3\text{-Fe}_2\text{O}_3\text{-420}$ and $\text{Al}_2\text{O}_3\text{-Fe}_2\text{O}_3\text{-550}$
94 samples were prepared in the same way, but sintered at higher temperatures of 420°C and
95 550°C for 2 h, respectively and named “ $\text{Al}_2\text{O}_3(0.7)\text{-Fe}_2\text{O}_3\text{-420}$ ”, “ $\text{Al}_2\text{O}_3(0.6)\text{-Fe}_2\text{O}_3\text{-420}$ ”,
96 “ $\text{Al}_2\text{O}_3(0.5)\text{-Fe}_2\text{O}_3\text{-420}$ ”, “ $\text{Al}_2\text{O}_3(0.4)\text{-Fe}_2\text{O}_3\text{-420}$ ”, “ $\text{Al}_2\text{O}_3(0.3)\text{-Fe}_2\text{O}_3\text{-420}$ ”, “ $\text{Al}_2\text{O}_3(0.2)\text{-Fe}_2\text{O}_3\text{-}$
97 420 ”, “ $\text{Al}_2\text{O}_3(0.1)\text{-Fe}_2\text{O}_3\text{-420}$ ”, “ $\text{Al}_2\text{O}_3(0.05)\text{-Fe}_2\text{O}_3\text{-420}$ ”; “ $\text{Al}_2\text{O}_3(0.7)\text{-Fe}_2\text{O}_3\text{-550}$ ”, “ $\text{Al}_2\text{O}_3(0.6)\text{-}$
98 $\text{Fe}_2\text{O}_3\text{-550}$ ”, “ $\text{Al}_2\text{O}_3(0.5)\text{-Fe}_2\text{O}_3\text{-550}$ ”, “ $\text{Al}_2\text{O}_3(0.4)\text{-Fe}_2\text{O}_3\text{-550}$ ”, “ $\text{Al}_2\text{O}_3(0.3)\text{-Fe}_2\text{O}_3\text{-550}$ ”,
99 “ $\text{Al}_2\text{O}_3(0.2)\text{-Fe}_2\text{O}_3\text{-550}$ ”, “ $\text{Al}_2\text{O}_3(0.1)\text{-Fe}_2\text{O}_3\text{-550}$ ”, and “ $\text{Al}_2\text{O}_3(0.05)\text{-Fe}_2\text{O}_3\text{-550}$ ”, respectively.

100 Alumina content is defined as the molar ratios of Al/(Fe+Al) from aluminum salt and ferric salt
101 in this investigation.

102

103 **2.2 Characterization of Fe_2O_3 and Al_2O_3 - Fe_2O_3 samples**

104 To determine the crystal phase composition of the prepared catalysts, X-ray diffraction
105 (XRD) measurement was carried out at room temperature using a Rigaku D/MAX-III A
106 diffractometer with CuK_{α} radiation ($\lambda = 0.15418$ nm). The accelerating voltage of 35 kV and the
107 emission current of 30 mA were used. The BET surface area, micropore surface area, and total
108 pore volume of all samples were measured by the Brunauer-Emmett-Teller (BET) method, in
109 which the N_2 adsorption at 77 K using a Carlo Erba Sorptometer was applied. The pore-size
110 distribution of the catalysts was determined by the Barrett-Joyner-Halenda (BJH) method [23,24].
111 Fourier transform infrared spectra of the catalysts were also recorded with a FT-IR spectrometer
112 (Bruker Optics EQUINOX 55) at room temperature [25].

113

114 **2.3 Experimental setup and procedures**

115 A Pyrex cylindrical photoreactor with an effective volume of 250 ml was used to conduct
116 photocatalytic degradation experiments, which is surrounded by a Pyrex circulating water jacket
117 to control the temperature at 25 ± 2 °C during the reaction. An 8-W UV lamp (Luzchem Research,
118 Inc.) with a main emission at 365 nm is positioned at the centre of the cylindrical vessel and used
119 for photoreaction under UV-A irradiation at the light intensity of 1.2 mW cm^{-2} . The photoreactor
120 is covered with aluminium foil to keep it away from any indoor light interference.

121

122 BPA chemical (2,2-bis(4-hydroxyphenyl)propane) with analytical grade was purchased
123 from Aldrich and used without further purification to prepare aqueous BPA solution. The
124 reaction suspension was prepared by adding 0.25 g of catalyst powder into 250 ml of aqueous
125 BPA solution. Prior to the photoreaction, the suspension was magnetically stirred in the dark for
126 30 min to establish an adsorption/desorption equilibrium between solution and solid catalyst first
127 and then was irradiated by the UV lamp with constant aeration. At the given time intervals, the
128 analytical samples were taken from the suspension with immediate centrifugation for 20 min and
129 then filtered with a 0.45 μ m Millipore filter to remove the particles. All samples were then
130 stored in the dark prior to analyses.

131

132 **2.4 Analytical Methods**

133 BPA in aqueous samples were analyzed by high pressure liquid chromatography
134 (Finnigan LCQ DUO), which consists of a gradient pump (Spectra System P4000), an

135 autosampler (Spectra System Tem AS3000) with a 20 μ l injection loop, and a photodiode array
136 UV detector (Spectra SYSTEM UV6000LP). A Pinnacle II column (C18, 5 μ m, 250 \times 4.6 mm
137 ID) was used for BPA separation with a mobile phase (70% HCN: 30% water) at a flow rate of
138 0.8 ml min⁻¹. The BPA concentration was determined by the UV detector at 278 nm. Total
139 dissolved Fe ions (TD-Fe) was analyzed by atomic absorption spectrometry.

140

141 **3. Results and Discussion**

142

143 ***3.1 The effect of alumina on the crystal structure of catalysts***

144 Three series of Al₂O₃-Fe₂O₃ samples including Fe₂O₃ samples were examined by XRD
145 and their XRD patterns are shown in Fig. 1. For the Al₂O₃-Fe₂O₃-300 series, while Fe₂O₃-300
146 sample showed 5 peaks (220, 311, 421, 511, and 440) attributable to maghemite and 3 peaks
147 (012, 104, and 113) attributable to hematite, based on the Joint Committee on Powder
148 Diffraction Standards, indicating a mixed crystal structure of maghemite and hematite, the
149 Al₂O₃-Fe₂O₃-300 samples showed a relatively weaker crystal structure of maghemite with an
150 increased fraction of alumina. Furthermore, it can be seen that while Al₂O₃(0.05)-Fe₂O₃-300,
151 Al₂O₃(0.1)-Fe₂O₃-300 and Al₂O₃(0.2)-Fe₂O₃-300 showed 5 strong peaks of maghemite,
152 Al₂O₃(0.3)-Fe₂O₃-300, Al₂O₃(0.4)-Fe₂O₃-300, and Al₂O₃(0.5)-Fe₂O₃-300 showed only 4 peaks
153 (220, 311, 511 and 440) with much lower intensity, and Al₂O₃(0.6)-Fe₂O₃-300 and Al₂O₃(0.7)-
154 Fe₂O₃-300 showed almost an amorphous structure. These results indicate that introducing
155 alumina could delay the crystallization of iron oxides during the sintering treatment.

156 For the Al₂O₃-Fe₂O₃-420 series, while the Fe₂O₃-420 sample showed a crystal structure
157 of almost hematite with 8 peaks (012, 104, 110, 113, 024, 116, 214, and 300), the Al₂O₃(0.05)-
158 Fe₂O₃-420 and Al₂O₃(0.1)-Fe₂O₃-420 samples showed a mixed structure of maghemite and
159 hematite with both types of peaks (012, 220, 104, 311, 113, 024, 116, 511, and 440), the
160 Al₂O₃(0.2)-Fe₂O₃-420, Al₂O₃(0.3)-Fe₂O₃-420, Al₂O₃(0.4)-Fe₂O₃-420, Al₂O₃(0.5)-Fe₂O₃-420 and
161 Al₂O₃(0.6)-Fe₂O₃-420 samples showed 4 peaks of maghemite (220, 311, 511 and 440), and the
162 Al₂O₃(0.7)-Fe₂O₃-420 sample showed almost an amorphous structure. These results indicate that
163 introducing alumina does not only delay the crystallization, but also could hinder the crystal
164 transformation of iron oxides from maghemite to hematite during sintering treatment.

165 For the Al₂O₃-Fe₂O₃-550 series, while the Fe₂O₃-550 and Al₂O₃(0.05)-Fe₂O₃-550
166 samples showed a typical structure of hematite with 8 peaks (012, 104, 110, 113, 024, 116, 214,
167 and 300), the Al₂O₃(0.1)-Fe₂O₃-550 and Al₂O₃(0.2)-Fe₂O₃-550 samples showed a mixed
168 structure of maghemite and hematite with the 9 peaks (012, 104, 113, 024, 116, 214, 300, 311
169 and 220), and the Al₂O₃(0.3)-Fe₂O₃-550, Al₂O₃(0.4)-Fe₂O₃-550, Al₂O₃(0.5)-Fe₂O₃-550, and

170 Al₂O₃(0.6)-Fe₂O₃-550 samples showed almost a crystal structure of maghemite only. In the
171 meantime, the Al₂O₃(0.7)-Fe₂O₃-550 sample remained its amorphous structure. From the above
172 results, it is clear that the increase of sintering temperature will enhance crystal transformation of
173 iron oxides from maghemite to hematite significantly. Furthermore, it can be indicated that the
174 existence of alumina would delay the crystallization of iron oxides and also might hinder the
175 crystal transformation of iron oxides from maghemite to hematite as well.

176 The three series of catalysts with different crystal structures are summarized in Table 1.
177 Therefore, no any peak presented was attributable to alumina or the solid solutions of Al₂O₃ and
178 Fe₂O₃. That implies that alumina should be amorphous structure. In fact, crystallized alumina
179 such as γ -Al₂O₃ might present under thermal treatment at 800°C and α -Al₂O₃ might present
180 under thermal treatment at 1000°C [19,20].

181

182 [Fig. 1]

183 [Table 1]

184

185 ***3.2 The effect of alumina on the BET surface area and pore size distribution of catalysts***

186 The BET surface area and the pore structure of different catalysts were determined from
187 nitrogen isothermal analyses. Their nitrogen adsorption-desorption isothermal curves are shown
188 in Fig. 2 (A for Al₂O₃-Fe₂O₃-300; B for Al₂O₃-Fe₂O₃-420 and C for Al₂O₃-Fe₂O₃-550). It can be
189 seen that the adsorbed nitrogen volume decreased with increased temperature significantly and
190 their isotherms had a combined shape of type I and type IV with two distinct regions: at a low
191 relative pressure, isotherms exhibited high adsorption, indicating that the catalysts contained
192 micropores (type I) [23,24,26,27]. In addition, the curves also exhibited hysteresis loops at a high
193 relative pressure, indicating the presence of micropores and also mesopores. The distribution of
194 these hysteresis loops depended on the content of alumina. The shape of the hysteresis loops are
195 of type H3.

196

197 **[Fig. 2]**

198

199 The results of pore size distribution for different catalysts are shown in Fig. 3 (A for
200 Al₂O₃-Fe₂O₃-300, B for Al₂O₃-Fe₂O₃-420, and C for Al₂O₃-Fe₂O₃-550). It can be seen that the
201 pore size distribution strongly depended on the alumina content and also sintering temperature.
202 Fe₂O₃-300 showed a mixture pore size of mesopores and macropores with a significant peak at
203 18.36 nm, while Fe₂O₃-420 showed a mixture pore size of mesopores and macropores with the
204 peak at 30.17 nm. For three series, all catalysts except for Fe₂O₃-300 and Fe₂O₃-420 showed a

205 mixture pore size of micropore, mesopores and macropores, while pore sizes distributed from 1
206 up to 160 nm, and pore volumes decreased significantly with the increase of pore sizes for other
207 catalysts.

208
209 The analytical data for the BET surface area, micropore surface area, and micropore
210 volume of different catalysts are also summarized in Table 1. It is clear that both the BET
211 surface area and micropore surface area of all catalysts are dependent on sintering temperature
212 and also alumina content and increased with increased amount of alumina content significantly,
213 but decreased with increased sintering temperature at the same content of alumina. These results
214 revealed that the Al_{0.7}-Fe₂O₃-300 catalyst had the largest BET surface area of 115.32 m² g⁻¹ and
215 also the highest micropore volume of 28.57 m² g⁻¹, while the Fe₂O₃-550 catalyst had the lowest
216 BET surface area of 7.82 m² g⁻¹.

217
218 [Fig. 3]

219 220 **3.3 The effect of alumina on the chemical state of catalysts**

221 The FTIR transmittance spectra from 4000 to 400 cm⁻¹ are shown in Fig. 4 (A for Al₂O₃-
222 Fe₂O₃-300, B for Al₂O₃-Fe₂O₃-420, and C for Al₂O₃-Fe₂O₃-550) to investigate the effect of
223 alumina on the chemical state of catalysts. For all catalysts, the broad peaks in the range of 3350-
224 3450cm⁻¹ and the narrow peak at about 1620 cm⁻¹ are attributable to the O-H stretching vibration
225 of water and an OH group on the surface of iron oxides. The peaks at 470 and 540 cm⁻¹ should
226 be attributable to the Fe-O vibration of hematite for Fe₂O₃-300, Fe₂O₃-420, Al₂O₃(0.1)-Fe₂O₃-
227 420, Fe₂O₃-550, Al₂O₃(0.1)-Fe₂O₃-550, and Al₂O₃(0.2)-Fe₂O₃-550, while the peaks at 560, 640,
228 and 696 cm⁻¹ should be attributable to the Fe-O vibration of maghemite, as labelled in Fig. 4
229 [8,18-20].

230
231 [Fig. 4]

232 233 **3.4 The effect of alumina on the photocatalytic degradation of BPA**

234 Under UV-A illumination, iron oxides can be excited to generate holes and electrons, and
235 the excited electrons are further transferred to oxygen to form hydroxyl radicals as described by
236 the equations 1-3. BPA in the reaction solution is then attacked by the hydroxyl radicals to be
237 degraded. To investigate the effect of alumina on the photocatalytic activity of iron oxides in
238 BPA degradation, three sets of experiments were carried out in aqueous BPA suspension with an
239 initial concentration of 0.044 mM and 1 g l⁻¹ of catalyst under UV-A illumination and each

240 experiment lasted for 150 min. The experimental results are shown in Fig. 5. By assuming that
241 the photocatalytic degradation of BPA in aqueous suspension follows the first-order kinetics, the
242 first-order kinetic constants, k , can be calculated by fitting the experimental data and are
243 compared in Table 2.

244

245 [Fig. 5]

246 [Table 2]

247

248 For the $\text{Al}_2\text{O}_3\text{-Fe}_2\text{O}_3\text{-300}$ series, it can be seen that while the $\text{Fe}_2\text{O}_3\text{-300}$ catalyst had the
249 highest k value, the $\text{Al}_2\text{O}_3\text{-Fe}_2\text{O}_3\text{-300}$ catalysts had lower k values that are decreased with
250 increased fraction of alumina. Since the $\text{Al}_2\text{O}_3\text{-Fe}_2\text{O}_3\text{-300}$ catalysts with higher fraction of
251 alumina were more amorphous, it implies that the higher crystalline of maghemite might lead to
252 the higher photocatalytic activity. For the $\text{Al}_2\text{O}_3\text{-Fe}_2\text{O}_3\text{-420}$ series and $\text{Al}_2\text{O}_3\text{-Fe}_2\text{O}_3\text{-550}$ series,
253 both the $\text{Al}_2\text{O}_3(0.1)\text{-Fe}_2\text{O}_3\text{-420}$ and $\text{Al}_2\text{O}_3(0.1)\text{-Fe}_2\text{O}_3\text{-550}$ catalysts had the highest k values in
254 their temperature series, respectively, which indicate that the iron oxides with 10% alumina had
255 the highest activity for BPA degradation under UV-A illumination. Comparing three series of
256 catalysts sintered at different temperatures, it is significant that the $\text{Al}_2\text{O}_3\text{-Fe}_2\text{O}_3\text{-420}$ series had
257 higher k values than the $\text{Al}_2\text{O}_3\text{-Fe}_2\text{O}_3\text{-300}$ and $\text{Al}_2\text{O}_3\text{-Fe}_2\text{O}_3\text{-550}$ series.

258 From the above experimental results, it may be summarized that although the
259 photocatalytic activity of iron oxides should depend on a number of their characteristics such as
260 crystalline, crystal structure, surface structure properties, surface area and so on. Among them,
261 the crystalline and crystal structure might play more critical roles than the surface structure
262 properties in BPA degradation under these experimental conditions. For the catalysts sintered at
263 a same temperature, the effect of alumina on photocatalytic activity might result from their
264 different crystalline and crystal structure. The experiments in this study demonstrated that the
265 catalysts containing a mixture of maghemite and hematite had the higher activity than those
266 containing either maghemite or hematite alone. Actually two band gaps of maghemite (2.03 eV)
267 and hematite (2.02 eV) are very close, but they have different positions. While hematite has a
268 conduction band level at -0.62 V and a valence band level at +1.40 V, maghemite has the two
269 band levels at -0.08 V and +1.94 V, respectively [10]. In their mixture, the excited electrons at
270 the conduction band of hematite would transfer to the conduction band of maghemite easily,
271 which results in an effective electron separation and transformation within the iron oxides.
272 Furthermore, the maghemite catalysts with a higher crystalline degree had the higher
273 photocatalytic activity.

274 It is well known that many iron oxides in an acidic solution can be dissolved by light
275 irradiation to release Fe³⁺ ion as shown below:

276



279

280 In this study, the concentration of total dissolved Fe (TD-Fe) during photoreaction was
281 determined by atom adsorption spectra (AAS) and the results are shown in Fig. 6. The
282 experiments demonstrated that most iron oxides released Fe³⁺ into the aqueous suspension
283 during the reaction and the TD-Fe concentrations were quickly increased after a short reaction
284 time and then gradually reached their maximum levels and maintained until the end of
285 experiments at 150 min. It can be seen that the iron oxides with 40%-60% alumina released
286 more Fe³⁺ than others for three series of catalysts sintered at different temperatures. In fact, such
287 a photo-dissolution of iron oxides depends on the crystalline and also crystal structure of iron
288 oxides. In general, maghemite is more easily photo-dissolved than hematite, and iron oxides with
289 higher crystalline are more difficult to be photo-dissolved than those with lower crystalline. On
290 the other hand, the degree of iron dissolution also depends on pH. The dominant specie in the
291 absence of organic ligand is Fe₂(OH)₂⁴⁺ in weak acidic solution, which could be further
292 photoreduced to form hydroxyl radical and Fe²⁺ as shown by reaction 5. However, the quantum
293 yield for the formation of hydroxyl radical is only 0.017 at 360 nm [28-30], the BPA degradation
294 under UV-A illumination at 365 nm was affected by the dissolution of iron oxides and the
295 formation of dissolved ferric ion at a minor degree for iron oxides with a higher crystalline and
296 activity, and at a significant degree for iron oxides with a lower crystalline under this
297 experimental condition. The excitation of dissolved ferric ion under UV-A illumination might
298 play a sole role in BPA degradation for catalysts with amorphous structure.

299

300 [Fig. 6]

301

302 4. Conclusions

303 It could be confirmed that the crystal structure and crystalline, the surface area and pore
304 size distribution of Al₂O₃-Fe₂O₃ catalysts depend strongly on the content of alumina and also
305 sintering temperature. The existence of alumina could hinder the crystallization of iron oxides
306 and also crystal transformation from maghemite to hematite during sintering. The BET surface
307 area and micropore surface area increased significantly with an increased content of alumina, but
308 decreased with an increased sintering temperature. The dependence of BPA degradation on the

309 alumina content was attributable to the crystal structure, crystalline and also the properties of
310 surface structures of Al₂O₃-Fe₂O₃ catalysts.

311

312 **Acknowledgement**

313 The authors would thank the Hong Kong Government Research Grant Committee for a
314 financial support to this work (RGC No: PolyU 5148/03E), and also would think China National
315 Natural Science Foundation (Project No.: 20377011) and Guangdong Natural Science
316 Foundation Key (Project No.: 036533).

317

318 **References**

- 319 [1] M. A. A. Schoonen, Y. Xu, D. R. J. Strongin, *Geochem. Exploration* 62 (1998) 201-215.
320 [2] F. E. Rhoton, J. M. Bigham, D. L. Lindbo, *Appl. Geochem.* 17 (2002) 409-419.
321 [3] C. Swearingen, S. Macha, A. Fitch, *J. Mol. Catal. A: Chem.* 199 (2003) 149-160.
322 [4] P. Behra, L. Sigg, *Nature* 344 (1990) 419-421
323 [5] T. J. Grundl, D. L. Sparks, Kinetics and mechanisms of reactions at the mineral-water interface: an
324 overview. In: D. L. Sparks, T. J. Grundl (eds), *Mineral-Water Interfacial Reactions: Kinetics and*
325 *Mechanisms*. American Chemical Society, Washington, DC, 1998. pp. 2-13.
326 [6] P. M. Huang, *Advances in Agronomy* 82 (2004) 391-472.
327 [7] F. Keppler, R. Eiden, V. Niedan, J. Pracht, H. F. Scholer, *Nature* 403 (2000) 298-301.
328 [8] R. M. Cornell, U. Schwertmann, *The Iron Oxides: Structure, Properties, Reactions, Occurrences and Uses*.
329 Wiley-VCH, New York. 2003.
330 [9] B. C. Faust, M. R. Hoffmann, D. W. Bahnemann, *J. Phys. Chem.* 93 (1989) 6371-6381.
331 [10] J. K. Leland, A. J. Bard, *J. Phys. Chem.* 91 (1987) 5076-5083.
332 [11] R. Andreozzi, V. Caprio, R. Marotta, *Water Res.* 37 (2003) 3682-3688.
333 [12] B. C. Faust, J. Allen, *Environ. Sci. Technol.* 27 (1993) 2517-2522.
334 [13] H. B. Fu, X. Quan, Z. Y. Liu, S. Chen, *Langmuir* 20 (2004) 4867-4873.
335 [14] C. Kormann, D. W. Bahnemann, M. R. Hoffmann, *J. Photochem. Photobio. A: Chem.* 48 (1989) 161-169.
336 [15] B. Pal, M. J. Sharon, *Chem. Technol. Biotechnol.* 73 (1998) 269-273.
337 [16] C. L. Hsueh, Y. H. Huang, C. Y. Chen, *J. Hazard. Mater.* B129 (2006) 228-233
338 [17] K. M. Cunningham, M. C. Goldberg, E. R. Weiner, *Environ. Sci. Technol.* 22 (1988) 1090-1097.
339 [18] M. A. Karakassides, D. Gournis, A. B. Bourlinos, P. N. Trikalitis, T. Bakas, *J. Mater. Chem.* 13 (2003)
340 871-876.
341 [19] E. A. El-Sharkawy, S. A. El-Hakam, S. E. Samra, *Mater. Lett.* 42 (2000) 331-338
342 [20] W. M. Shaheen, K. S. Hong, *Thermochimica Acta*, 381 (2002) 153-164
343 [21] I. T. Cousins, C. A. Staples, G. M. Klecka, D. Mackay, *Human and Ecological Risk Assessment* 8 (2002)
344 1107-1135.
345 [22] N. Watanabe, S. Horikoshi, H. Kawabe, Y. Sugie, J. C. Zhao, H. Hidaka, *Chemosphere* 52 (2003) 851-
346 859.

- 347 [23] J. G. Yu, J. C. Yu, M. K.-P. Leung, W., K. Ho, B. Cheng, X. J. Zhao, J. C. Zhao, *J. Catal.* 217 (2003) 69-
348 78.
- 349 [24] S. L. Gregg, K. S. W. Sing, *Adsorption, Surface Area and Porosity*, Academic Press, London. 1982.
- 350 [25] H. D. Ruan, R. L. Frost, J. T. Kloprogge, L. Duong, *Spectrochimica Acta Part A* 58 (2002) 967-981.
- 351 [26] J. Lei, C. S. Liu, F.B. Li, X. M. Li, S. G. Zhou, T. X. Liu, M. H. Gu, Q. T. Wu, *J. Hazard. Mater.*
352 137(2006) 1016–1024
- 353 [27] M. H. Zhou, J. G. Yu, B. Cheng, *J. Hazard. Mater.* 138(2006) 1838–1847
- 354 [28] Y. G. Zuo, J. Holgné, *Environ. Sci. Technol.* 26 (1992) 1014-1022.
- 355 [29] M. E. Balmer, B. Sulzberger, *Environ. Sci. Technol.* 33 (1999) 2418-2424.
- 356 [30] P. Huston, J. J. Pignatello, *Environ. Sci. Technol.* 30 (1996) 3457-3463.
- 357

Table 1 The crystal structure, BET surface area, micro pore surface area and micropore volume of iron oxides

Iron oxides	Al ₂ O ₃ (0.7)-Fe ₂ O ₃ - 300	Al ₂ O ₃ (0.5)-Fe ₂ O ₃ - 300	Al ₂ O ₃ (0.3)-Fe ₂ O ₃ - 300	Al ₂ O ₃ (0.2)-Fe ₂ O ₃ - 300	Al ₂ O ₃ (0.1)-Fe ₂ O ₃ - 300	Fe ₂ O ₃ -300
Crystal structure	amorphous	γ -Fe ₂ O ₃	γ + α -Fe ₂ O ₃			
BET surface area (m ² g ⁻¹)	115.32	88.46	87.25	81.36	63.37	26.93
Micropore surface area (m ² g ⁻¹)	28.57	7.45	4.56	3.65	2.38	1.27
Micropore volume (cm ³ g ⁻¹)	0.012	0.0033	0.00016	0.0029	0.0012	0.0003
Iron oxides	Al ₂ O ₃ (0.7)-Fe ₂ O ₃ - 420	Al ₂ O ₃ (0.5)-Fe ₂ O ₃ - 420	Al ₂ O ₃ (0.3)-Fe ₂ O ₃ - 420	Al ₂ O ₃ (0.2)-Fe ₂ O ₃ - 420	Al ₂ O ₃ (0.1)-Fe ₂ O ₃ - 420	Fe ₂ O ₃ -420
Crystal structure	amorphous	γ -Fe ₂ O ₃	γ -Fe ₂ O ₃	γ -Fe ₂ O ₃	γ + α -Fe ₂ O ₃	α -Fe ₂ O ₃
BET surface area (m ² g ⁻¹)	98.96	68.65	61.43	55.69	40.737	12.92
Micropore surface area (m ² g ⁻¹)	25.23	4.107	2.924	2.57	1.351	0.15
Micropore volume (m ³ g ⁻¹)	0.010	0.00066	0.00057	0.00071	0.0012	0.0000
Iron oxides	Al ₂ O ₃ (0.7)-Fe ₂ O ₃ - 550	Al ₂ O ₃ (0.5)-Fe ₂ O ₃ - 550	Al ₂ O ₃ (0.3)-Fe ₂ O ₃ - 550	Al ₂ O ₃ (0.2)-Fe ₂ O ₃ - 550	Al ₂ O ₃ (0.1)-Fe ₂ O ₃ - 550	Fe ₂ O ₃ -550
Crystal structure	amorphous	γ -Fe ₂ O ₃	γ -Fe ₂ O ₃	γ + α -Fe ₂ O ₃	γ + α -Fe ₂ O ₃	α -Fe ₂ O ₃
BET surface area (m ² g ⁻¹)	72.17	67.66	60.63	41.87	27.94	7.82
Micropore surface area (m ² g ⁻¹)	5.0455	2.3066	1.0396	0.7295	0	0
Micropore volume (m ³ g ⁻¹)	0.00223	0.00117	0.00059	0.00043	0	0

Table 2 The first-order kinetic constants k (min^{-1}) for BPA degradation under UV-A illumination using different catalysts

Catalysts	k	R^2	Catalysts	k	R^2	Catalysts	k	R^2
Fe ₂ O ₃ -300	0.0018	0.9928	Fe ₂ O ₃ -420	0.0034	0.9612	Fe ₂ O ₃ -550	0.0016	0.9689
Al ₂ O ₃ (0.05)-Fe ₂ O ₃ -300	0.0016	0.9710	Al ₂ O ₃ (0.05)-Fe ₂ O ₃ -420	0.0075	0.9959	Al ₂ O ₃ (0.05)-Fe ₂ O ₃ -550	0.0022	0.9773
Al ₂ O ₃ (0.1)-Fe ₂ O ₃ -300	0.0012	0.9982	Al ₂ O ₃ (0.1)-Fe ₂ O ₃ -420	0.0080	0.9988	Al ₂ O ₃ (0.1)-Fe ₂ O ₃ -550	0.0028	0.9882
Al ₂ O ₃ (0.2)-Fe ₂ O ₃ -300	0.0009	0.9817	Al ₂ O ₃ (0.2)-Fe ₂ O ₃ -420	0.0058	0.9958	Al ₂ O ₃ (0.2)-Fe ₂ O ₃ -550	0.0015	0.9655
Al ₂ O ₃ (0.3)-Fe ₂ O ₃ -300	0.0008	0.9905	Al ₂ O ₃ (0.3)-Fe ₂ O ₃ -420	0.0039	0.9612	Al ₂ O ₃ (0.3)-Fe ₂ O ₃ -550	0.0006	0.9662
Al ₂ O ₃ (0.4)-Fe ₂ O ₃ -300	0.0008	0.9690	Al ₂ O ₃ (0.4)-Fe ₂ O ₃ -420	0.0031	0.9585	Al ₂ O ₃ (0.4)-Fe ₂ O ₃ -550	0.0005	0.9625
Al ₂ O ₃ (0.5)-Fe ₂ O ₃ -300	0.0007	0.9480	Al ₂ O ₃ (0.5)-Fe ₂ O ₃ -420	0.0021	0.9967	Al ₂ O ₃ (0.5)-Fe ₂ O ₃ -550	0.0004	0.9832
Al ₂ O ₃ (0.6)-Fe ₂ O ₃ -300	0.0005	0.9569	Al ₂ O ₃ (0.6)-Fe ₂ O ₃ -420	0.0016	0.9928	Al ₂ O ₃ (0.6)-Fe ₂ O ₃ -550	0.0003	0.9848
Al ₂ O ₃ (0.7)-Fe ₂ O ₃ -300	0.0005	0.9818	Al ₂ O ₃ (0.7)-Fe ₂ O ₃ -420	0.0015	0.9916	Al ₂ O ₃ (0.7)-Fe ₂ O ₃ -550	0.0003	0.9858

List of figure captions

Fig. 1. The XRD patterns of different iron oxides sintered at 300 °C (A), 420 °C (B) and 550 °C (C).

Fig. 2. The nitrogen adsorption-desorption isothermal curves of Fe₂O₃-Al₂O₃ powders sintered at 300 °C (A), 420 °C (B) and 550 °C (C)

Fig. 3. The pore size distribution of Fe₂O₃-Al₂O₃ powders sintered at 300 °C (A), 420 °C (B) and 550 °C (C)

Fig. 4. The FTIR transmittance spectra of Fe₂O₃-Al₂O₃ powders sintered at 300 °C (A), 420 °C (B) and 550 °C (C)

Fig. 5. The photocatalytic degradation of BPA under UV-A illumination using different iron oxides sintered at 300 °C (A), 420 °C (B) and 550 °C (C)

Fig. 6. The photo-dissolution of different iron oxides sintered at 300 °C (A), 420 °C (B) and 550 °C (C) under UV-A illumination vs. reaction time.

Fig.1

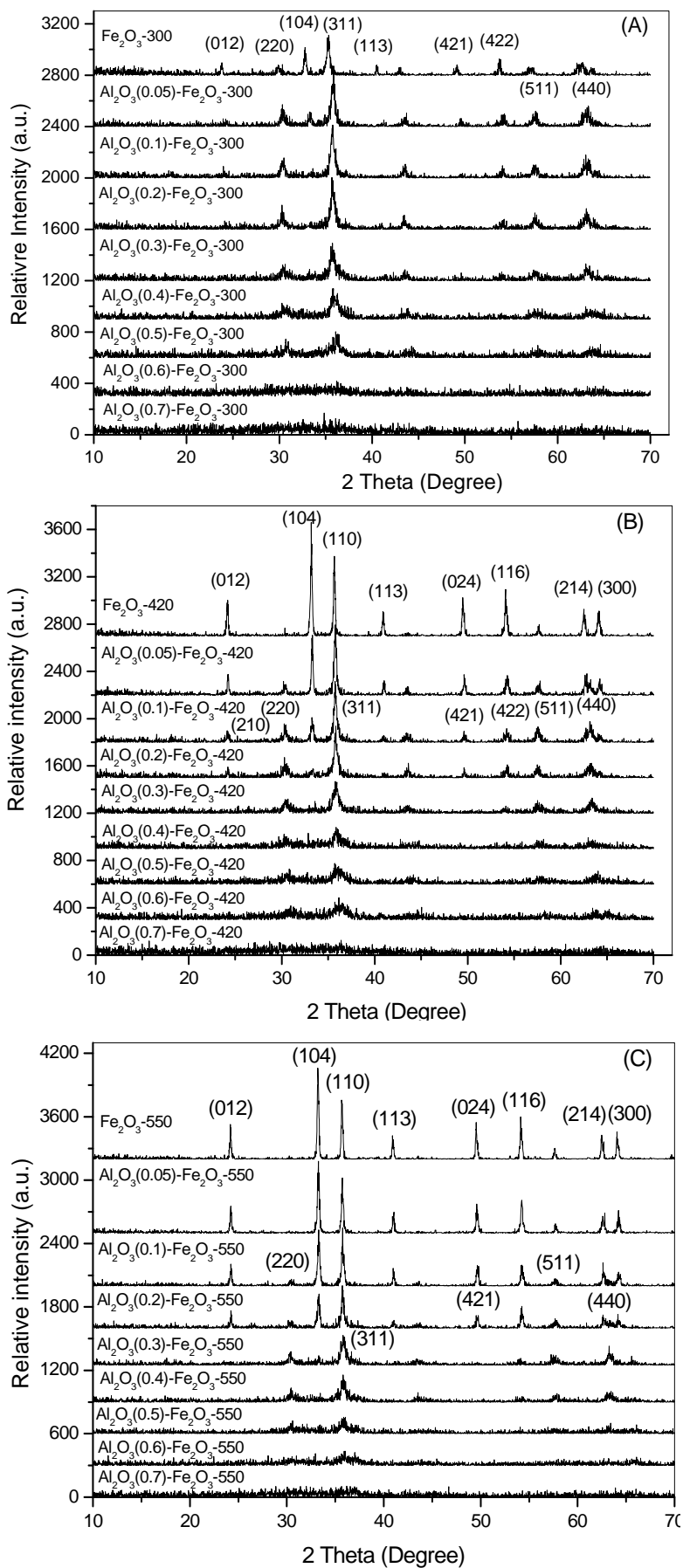


Fig. 2

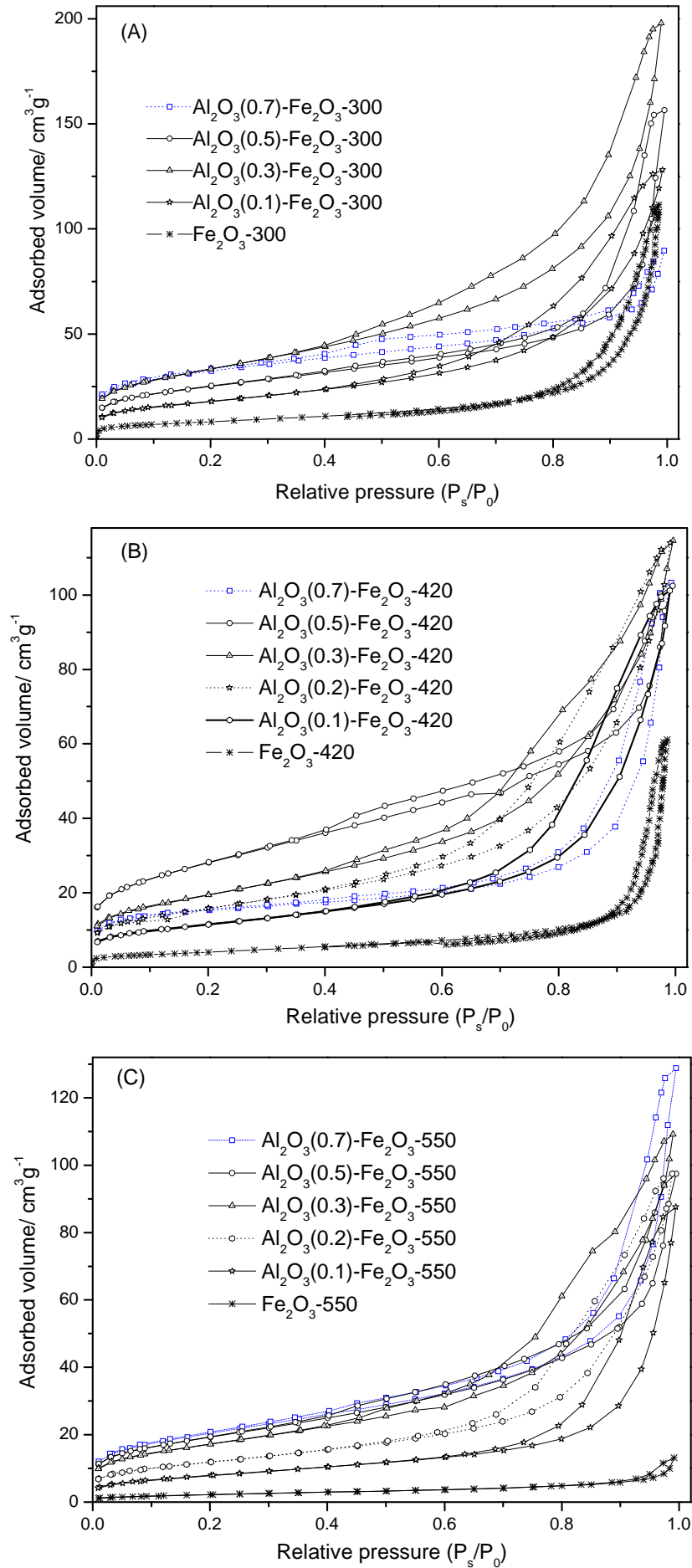


Fig. 3

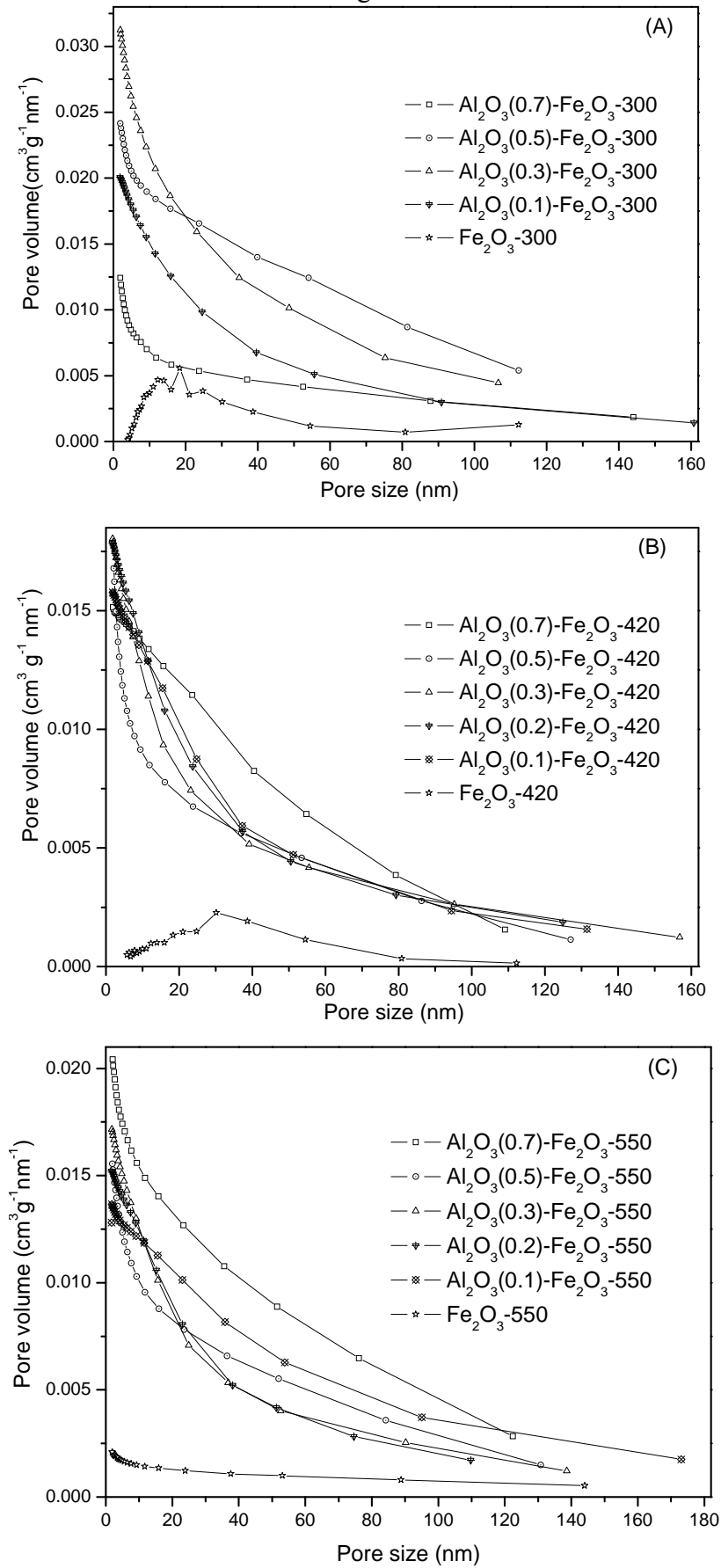


Fig. 4

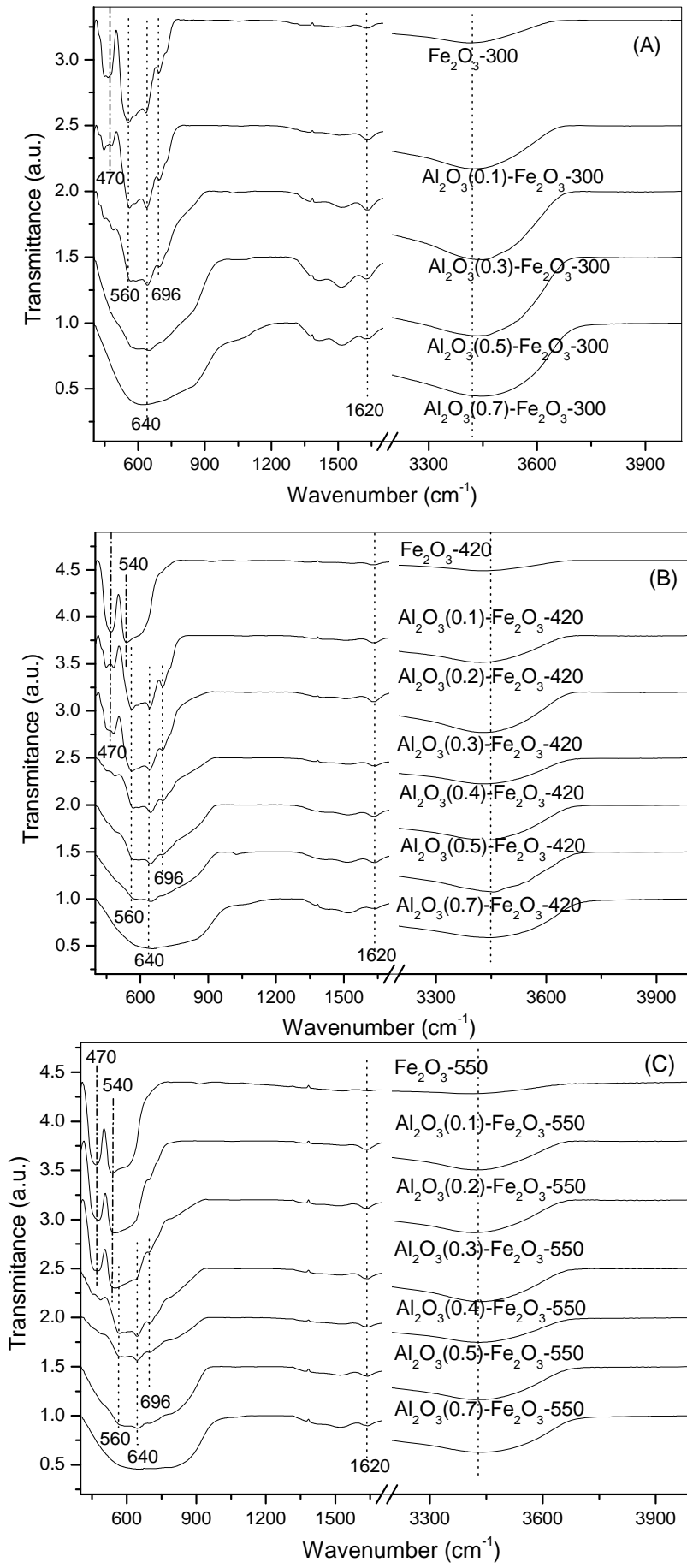


Fig. 5

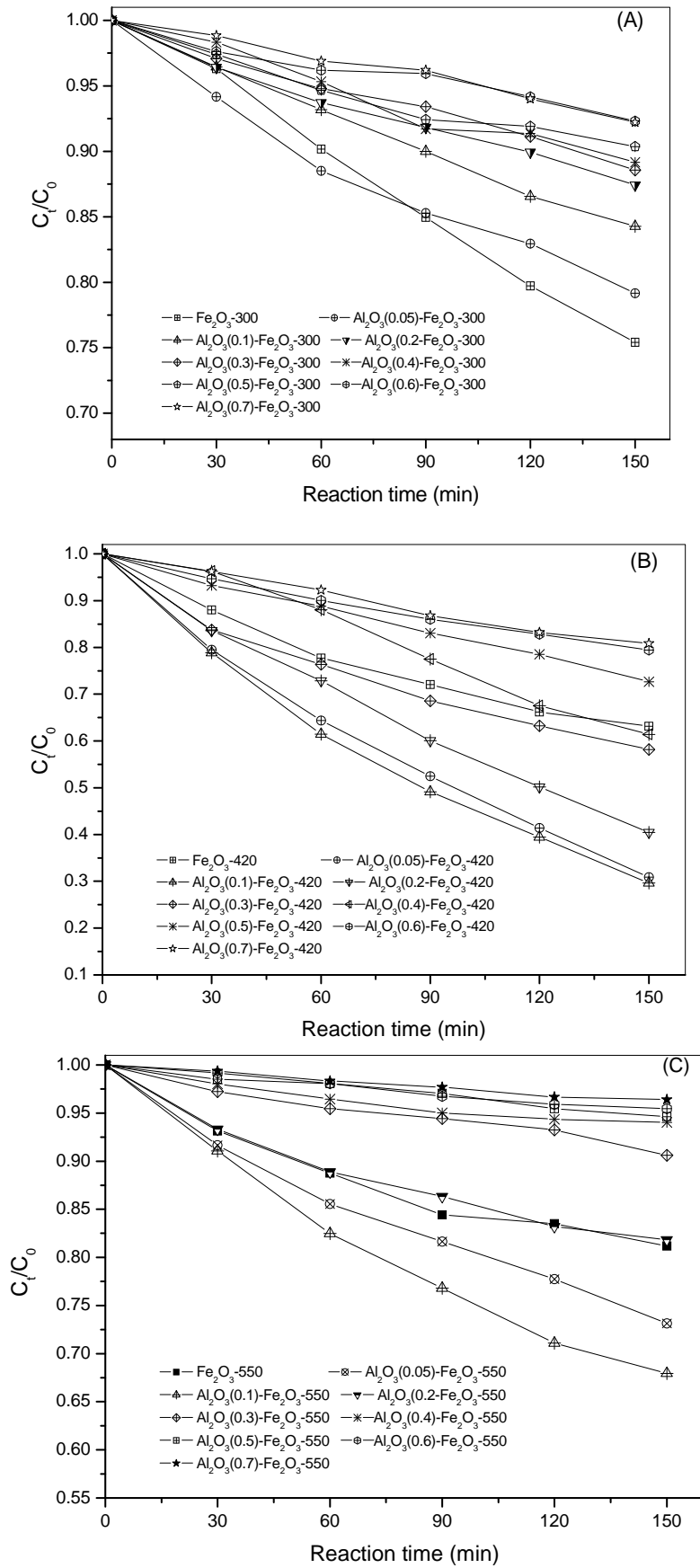


Fig. 6

